Electron injection effect in In2O3 and SnO2 nanocrystals modified by ruthenium heteroleptic complexes

Sergey Tokarev, Marina N. Rumyantseva, Abulkosim Nasriddinov, Alexandre M. Gaskov, Anna Moiseeva, Yury Fedorov, Olga Fedorova, Gediminas Jonusauskas

Electron injection effect in In_2O_3 and SnO_2 nanocrystals modified by ruthenium heteroleptic complexes

Sergey Tokarev,*[ab] Marina Rumyantseva,[b] Abulkosim Nasriddinov,[b] Alexander Gaskov,[b] Anna Moiseeva,[b] Yuri Fedorov,[a] Olga Fedorova*[ab] and Gediminas Jonusauskas[c]

In this work, the optical characteristics and conductivity under photoactivation with visible light of hybrids based on nanocrystalline SnO_2 or In_2O_3 semiconductor matrixes and heteroleptic Ru(II) complexes were studied. The heteroleptic Ru(II) complexes were prepared based on 1*H*-imidazo[4,5-*f*][1,10]phenanthroline and 2,2′-bipyridine ligands. Nanocrystalline semiconductor oxides were obtained by chemical precipitation with subsequent thermal annealing and characterized by XRD, SEM and single-point BET methods. The heteroleptic Ru(II) complexes as well as hybrid materials were characterized by time-resolved luminescence and X-ray photoelectron spectroscopy. The results showed that the surface modification of SnO_2 nanoparticles with heteroleptic ruthenium complexes led to an increase in conductivity upon irradiation with light appropriate for absorption by organometallic complexes. In the case of In_2O_3, the deposition of Ru(II) complexes resulted in a decrease in conductivity, apparently due to the special structure of the surface layer of the semiconductor.

Introduction

Polypyridine complexes of Ru(II) are widely studied as photosensitizers for photochemical and photoelectrochemical conversion of solar energy.[1] The favorable redox properties of the ^{3}MLCT state in $Ru(bpy)_3^{2+}$ and its relatively long lifetime are the main reasons behind its success as a photogalvanic converter,[2–4] as well as its involvement in the photoproduction of H_2 and O_2 from water.[3–5] The convenience of using mononuclear Ru(II) complexes to achieve these goals is due to the possibility of adjusting their optical and electrochemical properties in the ground and excited states by a reasonable choice of heterocyclic chelating ligands (ring size, substitution, and nature, number and position of the heteroatoms) and their relatively easy synthesis compared to multinuclear species. Even though considerable attention has been focused on derivatives of 2,2′-bipyridine with various peripheral substituents,[6,7] diazine ligands bearing two-ring N-heteroatoms have a lower energy of the lowest unoccupied molecular orbitals (LUMOs) as compared to many substituted bipyridines, which in turn gives rise to lower energy absorptions and emissions. Thus, the replacement of one of the bipyridine ligands by a diazine offers the possibility of tuning the redox and photophysical properties of the complexes. Ruthenium(II) complexes based on 3,3′-bipyridazine,[8] 2,2′-bipyrazine,[9] 2,2′-bipyrimidine,[10] and 4,4′-bipyrimidine[11] have been described in connection with their incorporation into solar energy conversion devices. Attention was also paid to complexes bearing the 4,4′-bipyrimidine ligand (bpm).[12,13]

Ligand modification and the use of different combinations of ligands are currently being pursued, in order to further investigate the potential of these complexes as photosensitizers, as well as the potential of free ligands as luminescent sensors.[14] One of the major objectives in the search for new photosensitizers has been the development of complexes that absorb in the visible spectrum, and maintain relatively long excited state lifetimes even if they emit at low energy.[15,16]

We suggest using imidazo[4,5-*f*][1,10]phenanthroline derivatives as ligands. These are compounds with an extended planar conjugated heteroaromatic system. The fragment of 1,10-phenanthroline is a strong binder for the Ru(II) cation.[17] Position 2 of the imidazole ring can be easily functionalized to configure electronic, optical and structural properties of ligands and their complexes. Ruthenium(II) complexes of imidazo[4,5-*f*][1,10]phenanthroline derivatives are usually chemically stable, absorb visible light and

[a] *A. N. Nesmeyanov Institute of Organoelement Compounds, Russian Academy of Sciences, 28 Vavilova str., 119991, Moscow, Russia. E-mail: tokarevsergeydm@yandex.ru, fedorova@ineos.ac.ru; Fax: +7 (499) 135 76 01*

[b] *Chemistry Department, M. V. Lomonosov Moscow State University, 119991 Moscow, Russia*

[c] *Laboratoire Ondes et Matière d'Aquitaine – UMR CNRS 5798, University of Bordeaux, 351 cours de la Libération, 33405 Talence, France. E-mail: gediminas.jonusauskas@u-bordeaux.fr*

have high lifetimes of the excited state.[18,19] They have been extensively studied in recent years as pH sensors and gas sensors for oxygen.[20,21] Such complexes are one of the most studied compounds for photodynamic therapy (PDT).[22,23] Clinical trials of the polypyridine Ru(II) complex with the imidazo[4,5-*f*]-[1,10]phenanthroline derivative as a drug for the photodynamic therapy of human bladder cancer were started in 2017. This is the first example of the real usage of transition metal organic complexes in such a type of treatment.[24]

Investigations on photoinduced charge-transfer between dye sensitizers and wide bandgap semiconductor films and particles are of considerable interest in the context of visible-region solar energy conversion (light-to-electricity conversion) *via* photoelectrochemical methods.[25,26] SnO_2 is a stable, wide band-gap semiconductor (E_g = 3.6 eV) that is widely used in many optoelectronic devices.[27] Numerous studies on dye injection into colloidal SnO_2 have been published,[28–31] and also significant works concerning dye-sensitized solar cells based on SnO_2 photoanodes have been presented.[32–40] Only a few works were devoted to In_2O_3 nanowires, which have been used for organic-semiconductor hybrid devices.[41–45]

In the present research, a series of Ru(II) complexes based on 1*H*-imidazo[4,5-*f*][1,10]phenanthroline derivatives (ImPh), and new hybrid materials obtained by covering SnO_2 and In_2O_3 nanoparticles with the reported Ru(II) complexes were studied using optical, photophysical, X-ray and electrochemical methods.

In the framework of the present research, the main goals were: (a) to determine the effect of the substituent in the imidazo-[4,5-*f*][1,10]phenanthroline ligand on the optical, photophysical and electrochemical characteristics of Ru(II) complexes as photosensitizers for semiconductor oxides; (b) to analyze the optical and photophysical characteristics of the organic–inorganic composites based on SnO_2 and In_2O_3 and the effect of organic modification on the conductivity of the semiconductor nanoparticles.

Synthesis of 1*H*-imidazo[4,5-*f*][1,10]-phenanthroline ligands and heteroleptic Ru(II) complexes

2-Substituted-1*H*-imidazo[4,5-*f*][1,10]phenanthrolines **1–4** and heteroleptic complexes **5–8** were prepared as shown in Scheme 1. The synthesis started with the oxidation of 1,10-phenanthroline with potassium bromate to give 1,10-phenathroline-5,6-dione as described in the literature.[46] Condensation reactions of the aldehydes with 1,10-phenathroline-5,6-dione gave ligands **1–4** as bright crystalline compounds with good yields .[47,48] Next, ligands were used to prepare the corresponding heteroleptic complexes **5–8** with *cis*-bis(2,2′-bipyridine)-dichlororuthenium(II) hydrate.[49] Accordingly, equimolar amounts of ligands **1–4** and $Ru(bpy)_2Cl_2$ were kept in ethanol at 80 °C in a sealed ampoule under argon for 8 h. After the reaction completed, the crude complexes were purified by column chromatography. Complexes **5–7** were described earlier.[50–52] The novel heteroleptic ruthenium complex **8** was unambiguously characterized by ^1H and ^{13}C NMR, MALDI-TOF mass spectrometry and elemental analysis

Optical and photophysical characteristics of Ru(II) complexes 5–8 in solution

The absorption spectra of complexes **5–8** in methanol are shown in Fig. 1.

The absorption bands located in the UV region are due to ligand-centered π–π* transitions. The 1*H*-imidazo-phenanthroline

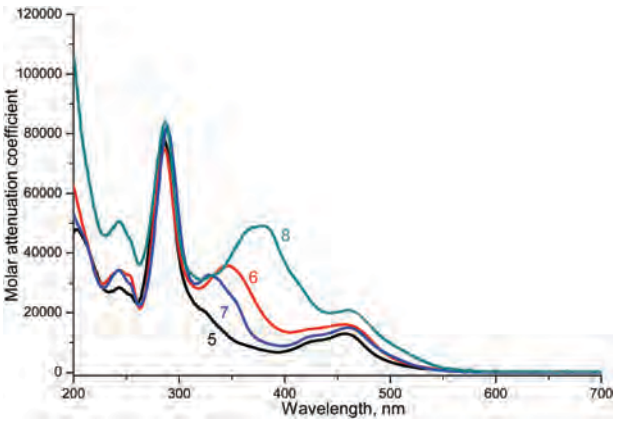

Fig. 1 Electronic absorption spectra of **5–8** in methanol, C_{5-8} = 1.5 × 10^{-5} M.

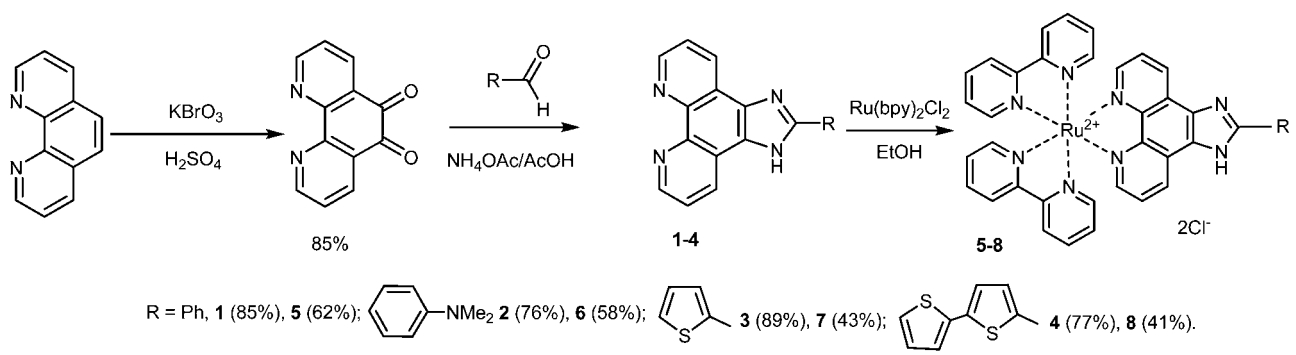

Scheme 1 Synthesis of ligands **1–4** and their Ru(II) complexes **5–8**.

Table 1 Spectroscopic data for **1–8** in air saturated and deoxygenated solutions

Compound	λ_{max}, nm	λ^{fl}_{max}, nm	Φ, O_2, % (Φ, degassed, %)	τ, ns (fraction, %), air saturated methanol	τ, ns (fraction, %), deoxygenated methanol
1	323	435	12.4	*	*
2	347	551	10.3	*	*
3	338	443	10.9	*	*
4	390	454	18.6	*	*
5	285, 322, 425, 457	608	1.36 (5.82)	201 (100)	939 (100)
6	286, 346, 425, 459	606	0.16 (0.43)	162 (100)	520 (35), 880 (65)
7	289, 327, 425, 460	605	0.64 (1.88)	120 (81), 231 (19)	462 (90), 1157 (10)
8	287, 380, 425, 462	614	0.02 (0.12)	198 (100)	957 (97), 15 400 (3)

*Not measured.

(ImPh) and pyridine π–π* transitions overlap at about 285 nm.[53] In addition, the π–π* transitions of substituted ImPhen residues are located in the region of 320–380 nm. This conclusion can be drawn when the absorption spectra of complexes **5–8** are compared with those of free ImPh ligands **1–4** (Table 1). An increase in the donor ability of the substituent in ImPh in complexes **5–8** leads to a long-wavelength shift of the band corresponding to the π–π* transition in the ligand. In the visible region, all complexes display wide absorption bands of the complex structures, which have been assigned to metal-to-ligand charge transfer (^{1}MLCT) transitions.

Complexes **6** and **8** in which the ImPh ligands contain an electron donating R group, namely dimethylamine or bithiophene residues, show a slight red-shift of the ^{1}MLCT in the region of 457–460 nm, compared to **5** and **7** respectively.

Previous studies have shown that electron-donating groups introduced in the heterocyclic ligands of Ru-complexes increase the σ-donating capacity of the ligand, destabilizing the Ru(dπ) orbitals and causing a red shift of the ^{1}MLCT maximum.[53]

Complexes **5–8** are all luminescent at room temperature. Luminescence spectra of **5–8** were obtained in methanol solution and the emission maxima, lifetimes and luminescence quantum yields are displayed in Table 1. The emission spectra of all complexes show a broad band with the emission maximum in the region of 608–614 nm. At room temperature, the emission intensity of ruthenium complexes decreases dramatically when going from **5** to **6** due to the dimethylamino-group that enhances interactions with the solvent, and especially from **7** to **8** due to an increase in the probability of competitive fast intersystem crossing or nonradiative relaxation with the addition of the thiophene unit.[54] The emission of the Ru(II) complexes can be attributed to the ^{3}MLCT transition.[55,56] The emission quantum yields are low in air saturated solution but increase substantially in deoxygenated methanol. It could be suggested that the photosensitization of molecular oxygen by the triplet excited states of Ru(II) complexes with the formation of singlet oxygen ($^1O_2$) takes place in air saturated solutions.[57–59]

For **5–8**, the corresponding lifetimes of exited states measured at the luminescence maximum in air saturated solution exceed 100 ns, while in deoxygenated methanol, the lifetimes increase up to 460–960 ns, which indicates the triplet nature of the excited state (Table 1). Complex **8** also has a longer lifetime (15.4 μs), which is likely due to reversible electronic energy transfer (REET) from the non-radiating ^{3}MLCT state associated with the ImPh ligand (see Fig. 2).[60]

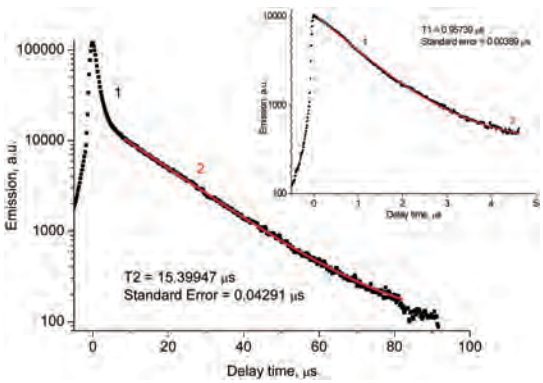

Fig. 2 Time-resolved emission decay of **8** (λ_{exc} = 450 nm), emission range: 550–700 nm, (1) in degassed methanol and the best monoexponential fit of long-lived luminescence component decay (2) in log scale. Inset: Time-resolved emission decay of **8** (the same solution and parameters as for 1) in degassed methanol on the scale from 0 to 5 μs and the best monoexponential fit of short-lived luminescence component decay (2) in log scale. T1, T2 – luminescence lifetimes.

Electrochemistry of ligands 1–4 and their Ru(II) complexes 5–8

The redox potentials of ligands **1–4** and heteroleptic complexes **5–8** determined by cyclic voltammetry in acetonitrile solution are summarized in Table 2.

Free ligands **1–4** demonstrate one-electron oxidation leading to the formation of imidazole cationic radicals that are easily polymerized on the surface of the electrode. In the series **1** → **3** → **4** → **2**, easier oxidation and more difficult reduction were observed from left to right, which correlates with the increasing donor character of substituents in the ImPh ligands (Table 2).

The voltammograms of complexes **5–8** contain three irreversible oxidation waves and three or four reduction waves. All observed electron reductions are ligand centered. The first two one-electron reductions of heteroleptic complexes **5–8** are reversible and relate to the reduction of ImPh, since ImPh is more easily reduced than 2,2′-bipyridine. During two sequential

Table 2 Electrochemical data and calculated values of HOMOs and LUMOs of **1–8** in MeCN with 0.1 M TBAP as the supporting electrolyte; potentials were measured relative to the Ag|AgCl|KCl aq. sat. reference electrode

Compound	$E_{1/2}$(red),[a] V	$E_{1/2}$(ox),[b] V	E_{HOMO}, eV	E_{LUMO}, eV
1	−1.23	1.22	−5.95	−3.50
2	−1.63	0.81	−5.54	−3.10
3	−1.30	1.04	−5.77	−3.43
4	−1.39	0.93	−5.66	−3.34
5	−1.26/−1.20	1.13	−5.86	−3.47
	−1.48/−1.40	1.37		
	−1.72 low	1.48		
	−1.96			
6	−1.18/−1.12	1.01	−5.74	−3.55
	−1.35/−1.30	1.34		
	−1.61	1.47		
	−1.94			
7	−1.30/−1.24	1.10	−5.83	−3.43
	−1.51/−1.45	1.37		
	−1.97/−1.87			
8	−1.27/−1.21	1.23	−5.96	−3.46
	−1.48/−1.41	1.42		
	−1.96/−1.84	1.52		

one-electron reductions, stable-in-time $Ru^{2+}[(bpy)_2ImPh]^{-\bullet}$ and $Ru^{2+}[(bpy)_2ImPh]^{2-}$ are formed. The third reduction potential for complexes **5–8** is about −1.96 V, which is very close to that obtained for $[Ru(bpy)_3]^{2+}$ and is assigned to the reduction of the bpy ligand.[61]

The oxidation waves for complexes **5–8** are irreversible. The first oxidation potentials ranging from +1.01 to +1.23 V for the heteroleptic complexes **5–8** could be attributed to the one-electron oxidation of the metal-centered HOMO (Table 2). We used the first oxidation potential for calculating the HOMO energy from electrochemical data. The second and third oxidation waves possibly correspond to the oxidation of two chloride anions in the same way as was shown in the literature.[62]

An effective electron transfer from the exited dye molecule can proceed only if its LUMO lies above the minimum of the conduction band of the semiconductor and the HOMO is located between the conduction and the valence bands. The relative positions of the molecular orbitals of the complexes and valence and conduction bands of semiconductor oxides calculated from the electrochemical data according to the literature[63] are shown in Fig. 3. The difference between the LUMO of the dye and the conduction band minimum (CBM) for SnO_2 is 0.5 eV larger than that for In_2O_3, which is expected to lead to more efficient electron transfer to tin oxide.

Interphase electron transfer in hybrid samples

At the next stage, complexes **5–8** were deposited on the surface of a semiconductor matrix to study the injection of electrons from organometallic compounds into the conduction band of the semiconductor metal oxides. Surface impregnation of tin and indium oxides was achieved by adding a methanol solution of the complex to the oxide powders, stirring the resulting suspension and evaporating the solvent. The concentration of

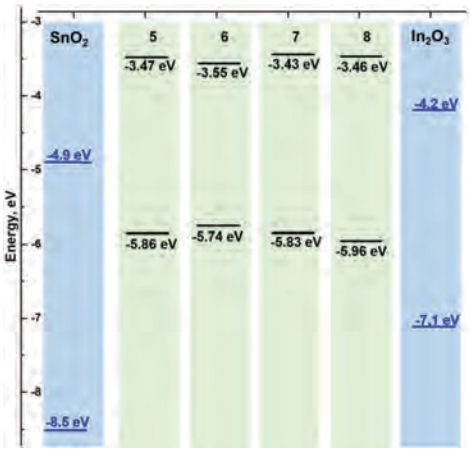

Fig. 3 Mutual arrangement of HOMO–LUMO levels of **5–8** and valence and conduction bands of semiconductor oxides.

the solution was adjusted so that the Ru content in the composites was 5 wt%. It is noteworthy that a red color of the surface was achieved immediately after adding the complex solution, confirming the dye grafting on the semiconductor surface. A detailed experimental procedure of SnO_2 and In_2O_3 surface modification has been described earlier.[64] According to the results of X-ray fluorescence analysis (XRF) for hybrids of complex **8**, the molecules of the heterocyclic ruthenium complexes were distributed evenly on the surface of the semiconductor oxides . The average content of ruthenium on SnO_2 and In_2O_3 surfaces in hybrid materials was [Ru]/([Ru] + [M]) = 1–5 at% (M = Sn and In) (Table 3) obtained *via* energy-dispersive X-ray spectroscopy (EDX). Then, the obtained hybrid materials were used to prepare colloidal suspensions in *n*-butanol. The resulting suspensions were placed on the surface of a glass plate and the solvent was evaporated in air for two hours.

Absorption spectra of SnO_2, In_2O_3, SnO_2 modified with **6**, and In_2O_3 modified with **6** are presented in Fig. 4. As one can see from Fig. 4, SnO_2 and In_2O_3 nanoparticles are transparent to visible light, with a strong optical absorption under ultraviolet light that has been interpreted as a direct band gap.[65] Thus, SnO_2 possesses an intensive band at λ_{max} 267 nm (E = 4.64 eV) and In_2O_3 demonstrates an intensive peak at λ_{max} = 305 nm (E = 4.06 eV). A weaker absorption of In_2O_3 at a higher energy (λ_{max} = 267 nm, E = 4.64 eV) has been early interpreted as an indirect band gap with the valence band maximum (VBM) away from the Γ-point.[66] In hybrids **6**-SnO_2 and **6**-In_2O_3 the absorption bands of heterocyclic Ru(II) complexes at 288 nm and 350 nm (Fig. 4) overlap with wide bands at 267 nm (**6**-SnO_2) and at 305 nm (**6**-In_2O_3), respectively. The bands in the region of 455–462 nm

Table 3 Elemental composition of the surface of sensitized composites

	5-SnO_2	**6**-SnO_2	**7**-SnO_2	**8**-SnO_2
[Ru]/([Ru] + [Sn]), at%	1.5 ± 0.1	1.3 ± 0.1	3.0 ± 0.3	1.4 ± 0.1
	5-In_2O_3	**6**-In_2O_3	**7**-In_2O_3	**8**-In_2O_3
[Ru]/([Ru] + [In]), at%	2.2 ± 0.2	2.2 ± 0.2	4.6 ± 0.4	2.1 ± 0.2

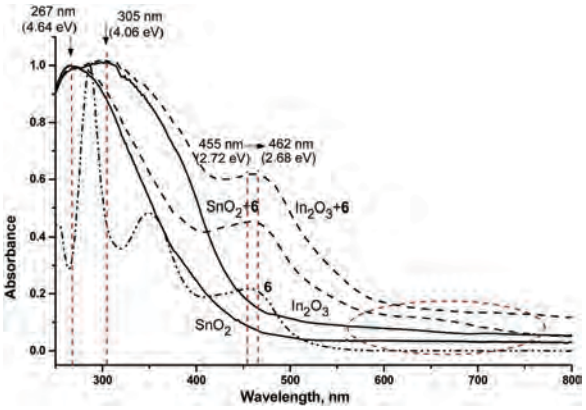

Fig. 4 Absorption spectra of **6**, SnO_2, and In_2O_3 free and modified with **6**.

belong to the Ru(II) complex and indicate its presence in the hybrid samples. The shoulder in the region of 600–710 nm may indicate a chemical interaction of the Ru(II) complex with the semiconductor oxide.

The prepared thick films of hybrid samples were studied by means of time-resolved luminescence spectroscopy.

Fig. 5 (top) shows the luminescence decay of 7-SnO_2 film on a 5 μs scale. Two luminescence decay components can be seen: a short-lived component in the region of 560–620 nm and a long-lived component with a maximum at about 670 nm. The photon energy of the long-lived luminescence component is 1.85 eV.

Fig. 5 (bottom) shows how the shape of the spectra and the position of the maximum change when moving an integration period along the luminescence decay map of Fig. 5 (top). The more time that passes from the beginning of the emission, the more the short-lived "blue" component decays and the long-lived "red" one appears. The intensity of the long-lived component is much lower, so the spectra with high delay are noisier.

The red-shifted luminescence component is more intense for all In_2O_3-based hybrids than for those of tin oxide. It should be emphasized that a temporal resolution on the scale of 5 μs is not enough for the spectrum of the blue-shifted component to be reliably recorded.

The blue components of the luminescence of **5–8** were resolved at a time scale of 50 ns; the spectrum of this short-wave emission component of the 7-SnO_2 composite is shown in Fig. 6 (bottom). It is remarkable that the shape and the position of the peak completely coincide with the luminescence spectrum of complex **7** in methanol solution; therefore, we assign the blue

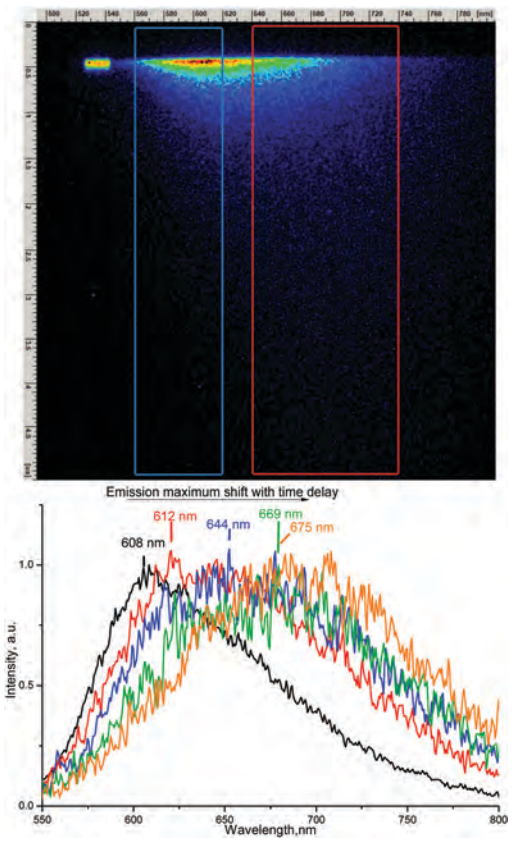

Fig. 5 (top) Luminescence decay map of **7**-SnO_2 thick film on glass on 5 μs scale, exc. = 460 nm; (bottom) the normalized spectra obtained from the luminescence decay map by integrating the intensity over wavelengths in periods of 0.4–0.9 μs (black), 0.9–1.4 μs (red), 1.4–1.9 μs (blue), 1.9–2.4 μs (green), and 2.4–2.9 μs (orange).

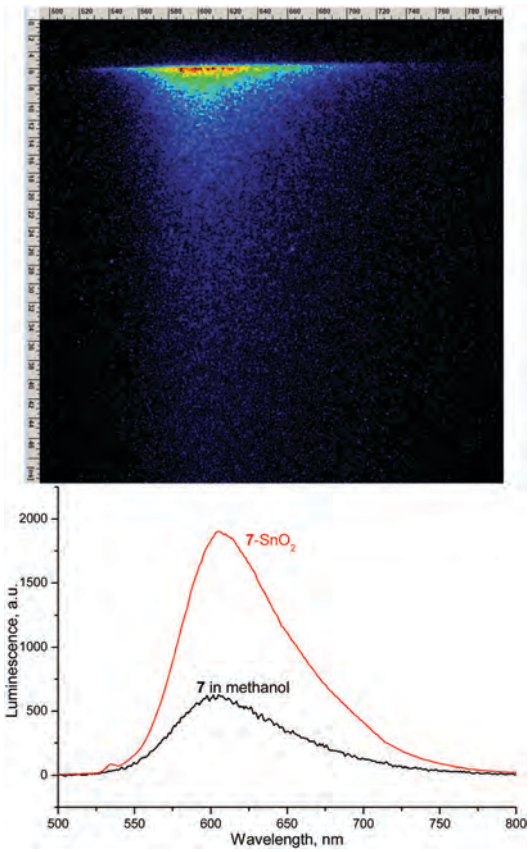

Fig. 6 (top) Luminescence decay map of **7**-SnO_2 thick film on glass on 50 ns scale, exc. = 460 nm; (bottom) luminescence spectrum of **7** in methanol (black) and spectrum of the blue-shifted component of **7**-SnO_2 obtained from the map by integrating the intensity over wavelengths in the period of 50 ns (red).

emission component of the 7-SnO_2 hybrid to the phosphorescence from the ^{3}MLCT excited state of complex 7. A similar emission pattern is observed for all hybrid materials.

According to the literature,[67,68] in SnO_2 and In_2O_3 nanoparticles, there are many defects causing the formation of additional energy levels (donor or acceptor) in the band gap of the semiconductor. Many theoretical studies emphasized the presence of donor defects near the conduction band minimum (CBM) of In_2O_3.

However, different authors report various positions of such defects relative to the CBM that are at 0.055 eV and 0.094 eV,[69] about 0.7 eV,[70] *etc.* Acceptor defects were also described,[71,72] but their exact position in the band gap was not indicated. J. D. Prades with colleagues[73] estimated the level of donor defects of SnO_2 nanoparticles as lying at 0.15–0.3 eV below the CBM, as well as two surface acceptor levels at 2.2 and 2.7 eV below the CBM.

Irradiation of the Ru(II) complex deposited on the surface of the semiconductor metal oxide causes first the CT singlet excited state that subsequently transforms into the ^{3}MLCT-triplet state. From the triplet state, two competitive processes are possible: (1) phosphorescence and relaxation to the ground state and (2) electron transfer to the conduction band of the semiconductor matrix. We assumed the following scheme of the process that occurs in hybrid materials upon the absorption of light (Fig. 7).

After the electron is transferred onto the surface of the semiconductor, it consistently relaxes to the donor defect levels, from which it is finally captured by surface acceptor defects with the emission of a photon (Fig. 7). We attributed this emission to "red" luminescence recorded in time-resolved experiments (number 3 in Fig. 7). This assumption was made because in SnO_2 nanoparticles, the difference between donor and acceptor defects is about 2.05–1.90 eV, as was shown earlier in the above cited references. Also, this assumption is in good agreement with the experimentally obtained emission wavelength of 660–680 nm. The proposed process suggests the oxidation of Ru(II) or the formation of radical particles as a result of photosensitization. It is possible that some close to the surface donor defects may contribute to the reduction of organic dyes, but the concentration of such defects should be low.

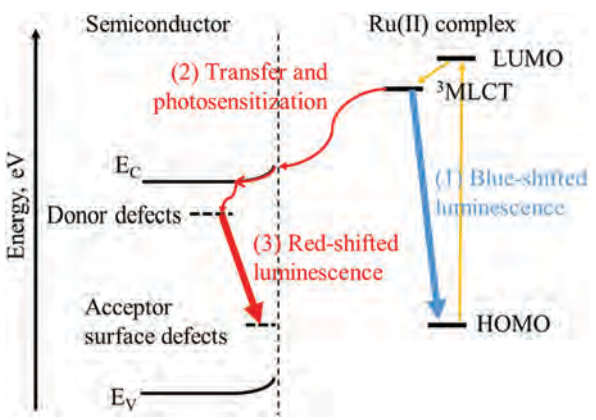

Fig. 7 Energy diagram illustrating processes occurring after excitation of ruthenium(II) complexes **5–8** on the surface of SnO_2.

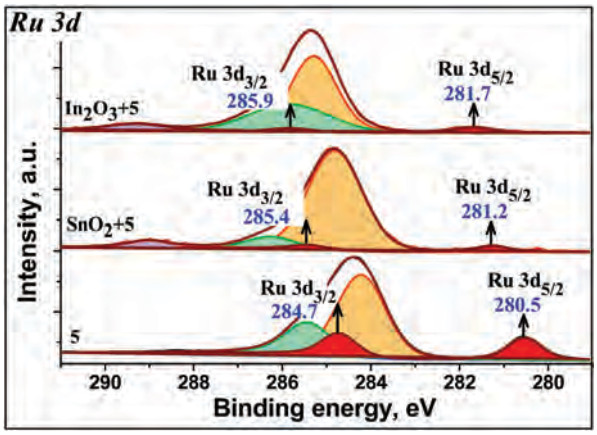

Fig. 8 X-ray photoelectron spectra of the Ru 3d element for complex **5** and its hybrid materials.

Incomplete recovery of the complex charge is confirmed by X-ray photoelectron spectroscopy (XPS). The high resolution spectrum in Fig. 8 shows the characteristic XPS core levels of Ru 3d and C 1s lines of the organometallic dye **5**. The intensive XPS peak was deconvoluted into three components (marked by orange, green and purple), which can be assigned to the different chemical states of carbon and Ru in the dye molecule.[74,75]

The low intensive and wide peaks observed at 280.5 eV and 284.7 eV belong to the Ru $3d_{5/2}$ and Ru $3d_{3/2}$ spin–orbit components, respectively, confirming the Ru^{2+} oxidation state.[76–79] The peak at 284.7 eV arises from the overlap of Ru $3d_{3/2}$ and C 1s peaks coming from molecule **5**. This is why the spectrum is difficult to calibrate and analyze accurately. The positions of Ru 3d peaks in the XP-spectra of **5**-SnO_2 and **5**-In_2O_3 samples are shifted to a higher binding energy by 0.7 and 1.2 eV, respectively, compared to that of the initial dye **5** (Fig. 8). This should be because the charge transfer between the Ru^{2+} complex and SnO_2 and In_2O_3 causes the partial oxidation of Ru^{2+} to Ru^{3+} or Ru^{4+}.[76,80–83]

As the electron transfer process is not radiative, it cannot be directly detected by optical methods. Therefore, its efficiency can be estimated by analysis of the blue-shifted luminescence decay rate. The shorter the lifetime of the emission component, the more effective the electron transfer to the conduction band of the semiconductor. To assess the effectiveness of photosensitization, we determined the shortest lifetime of the emitting excited state of the obtained hybrid materials on a scale of 50 ns, during which a rapidly decaying short-wavelength component of radiation can be resolved (Table 4

). In order to cut off the long-wavelength component, the integration over time was carried out at the wavelength of 560–620 nm.

Table 4 Lifetimes of short-lived components for hybrid materials in ns, $\lambda_{exc.}$ = 460 nm

	5	**6**	**7**	**8**
SnO_2	3.1	1.3	1.8	0.7
In_2O_3	3.9	2.0	2.3	0.9

To make sure that the blue emission component is not the luminescence of surface defects or the light scattered from the sample, we examined the luminescence decay of the unmodified semiconductor samples. The results showed that their luminescence differs markedly from the emission of the hybrid materials . Thus, we can evaluate the electron transfer efficiency from the emission of the hybrid samples.

The obtained phosphorescence lifetimes of the hybrid materials are 50–100 times lower than the phosphorescence of **5–8** in air-saturated solutions. Such very small values of emission lifetime clearly indicate that the emission of Ru complexes from ^{3}MLCT was inhibited with high efficiency by the competitive electron transfer into the surface of the semiconductor. Complex **8** demonstrates the best photosensitizing ability. The donor ability of the ImPhen ligand increases in the series **5** → **7** → **6** → **8**, and so in the same sequence, the electron transfer efficiency improves. Electron transfer to In_2O_3 is more complicated compared to SnO_2 for all organic dyes. Probably, the reason is the higher electron density near the conduction band of indium oxide. Indeed, according to the literature,[65] the Fermi level of In_2O_3 is located 0.02 eV above the CBM, indicating a downward bending of the conduction and valence bands at the surface, leading to an increase in electron density in the near-surface region. Evidently, electron transfer to a partially occupied conduction band is more difficult than to a free one.

Studies on the conductivity of hybrid materials and unmodified semiconductor nanoparticles proved the effectiveness of SnO_2 photosensitization. The resistances of different samples under irradiation with a blue 470 nm LED are listed in Table 5. All hybrid materials with tin oxide exhibited a significant decrease of resistance when irradiated with blue light. At the same time, all organic dyes deposited on indium oxide surface caused a conductivity reduction when irradiation was applied to the surface of hybrid samples compared to unmodified one.

As pointed out by P. D. C. King with colleagues,[71] indium oxide is an n-type semiconductor with shallow impurity levels that make possible the n-type conductivity already occurring at room temperature. The band structure of In_2O_3 and HOMO–LUMO energetic positions of complexes with respect to the Fermi level produce the bending of semiconductor bands to lower energies at the contact point and, as a consequence, the accumulation of electrons at the surface level. The tin oxide possesses n-type conductivity also. Yet, the position of all energetic levels in the hybrids produces the bending of SnO_2 bands to higher energy with a depletion of the conduction band electron population at the contact points with Ru complexes.[84]

Table 5 Resistance (MOhm) of pure semiconductor matrices and hybrid materials under irradiation with light at 470 nm at room temperature in pure air

Sample	In_2O_3	In_2O_3·**5**	In_2O_3·**6**	In_2O_3·**7**	In_2O_3·**8**
R, MOhm	0.013	3.7	2.1	2.3	0.36
Sample	SnO_2	SnO_2·**5**	SnO_2·**6**	SnO_2·**7**	SnO_2·**8**
R, MOhm	26.2	14.7	2.5	6.5	0.8

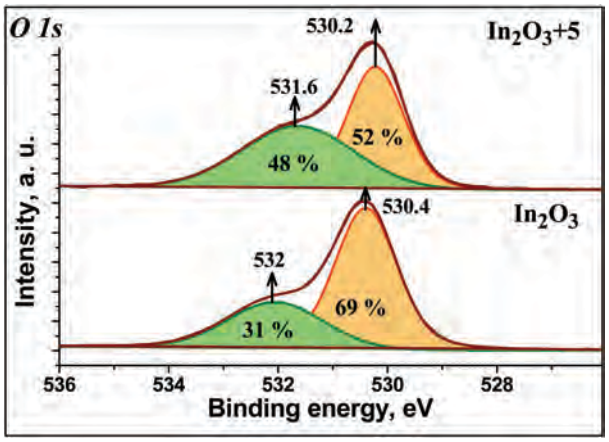

Fig. 9 X-ray photoelectron spectra of the O 1s element for complex **5** and its hybrid material.

Due to the characteristics mentioned above, the injection of additional electrons into the In_2O_3 surface layer from the photosensitizer is difficult. When it occurs, the charge carriers do not transfer into the bulk of the semiconductor but remain in the surface layer due to the band bending. The electron transferred from the dye to the In_2O_3 surface is captured by adsorbed oxygen, so it cannot contribute to the conductivity increase. As was mentioned, there are a large number of donor defects located close to the surface of In_2O_3 nanoparticles. Their energy level is slightly lower than the level of the conduction band of the semiconductor oxide and higher than the HOMO level of the dye, so defects easily donate electrons to the oxidized organic molecule restoring its charge. Thus, the defects cease to participate in the conductivity that leads to the increase of the resistance of the hybrid sample compared to the unmodified indium oxide.

Fig. 9 shows the O 1s XP-spectra of nanocrystalline In_2O_3 and **5**-In_2O_3 hybrid samples.

The deconvolution of the O 1s peak exhibited two oxygen components with binding energies at 530.4 and 532 eV. The first one, at 530.4 eV, is attributed to the lattice oxygen ions in the In_2O_3 structure, and the second one belongs to the surface chemisorbed oxygen and OH^- groups.[85–87]

It was observed that modification of In_2O_3 with complex **5** leads to an increase in the contribution of the higher energy O 1s component from 31% to 48% suggesting that more surface chemisorbed oxygen was formed in the hybrid sample. The shift of the maximum of the high energy O 1s component to a region with a lower binding energy can be explained by electron transfer from the Ru(II) complex (Ru 3d orbitals).

Experimental

Synthesis of hybrid materials

The powders of nanocrystalline SnO_2 and In_2O_3 were prepared, from $SnCl_4{\cdot}5H_2O$ and $In(NO_3)_3{\cdot}4.5H_2O$, respectively, using a chemical precipitation method.[88] After the stages of washing and drying, the products were annealed in air at 300 °C for 24 h.

Hybrids based on the semiconductor oxides and complexes **5–8** were prepared in the form of powders. First, the Ru-complex was dissolved in methanol; then, 10 μL of the obtained solution was added dropwise to a weighed sample of the semiconductor oxide and the paste was dried until the solvent was completely evaporated. The concentration of the solution was selected so that the Ru content in the hybrids was 1 wt%.

Material characterization

The composition of hybrid materials was investigated *via* EDX using a Zeiss NVision 40 (Carl Zeiss) microscope equipped with an X-Max detector (Oxford Instruments). The distribution of elements (Sn, In, and Ru) in hybrid samples was studied by using X-ray fluorescence (XRF) analysis using a high performance XRF micro spectrometer (Tornado M4 plus, Bruker) with a Rh anode (50 kV, 600 μA in mapping mode). The spot diameter was 18 microns. The distance between contact points was set to 20 microns. The results were obtained for the Kα lines of ruthenium, indium, and tin.

Absorption and emission spectra

UV-vis spectra were recorded using Varian-Cary 300, Varian-Cary 5G and Avantes AvaSpec-2048 spectrophotometers. Luminescence spectra were measured at 20 ± 1 °C with FluoroLog-3-221 (Horiba Scientific) and Agilent Cary Eclipse spectrofluorometers.

Luminescence quantum yield

All measured luminescence spectra were corrected for the non-uniformity of detector spectral sensitivity. Tris(2,2′-bipyridyl)-ruthenium(II) (ϕ_{fl} = 0.028) in ethanol was used as a reference for the luminescence quantum yield measurements. The luminescence quantum yields were calculated using the equation

$$\phi_i = \phi_0 \frac{(1 - 10^{-A_0}) \times S_i \times n_i^2}{(1 - 10^{-A_i}) \times S_0 \times n_0^2},$$

where ϕ_i and ϕ_0 are the luminescence quantum yields of the studied solution and the standard compound, respectively; A_i and A_0 are the absorptions of the studied solution and the standard, respectively; S_i and S_0 are the areas underneath the curves of the luminescence spectra of the studied solution and the standard, respectively; and n_i and n_0 are the refractive indices of the solvents for the substance under study and the standard compound (n_i = 1.3288, acetonitrile; n_0 = 1.361, ethanol).

Emission decay curves for solutions

The luminescence excitation light pulses for the time-resolved measurements were obtained by frequency doubling and tripling of a Ti:sapphire femtosecond laser system (Femtopower Compact Pro) output. The depolarized excitation light was used to excite the samples. The highest pulse energies used to excite emission did not exceed 100 nJ and the average power of the excitation beam was 0.1 mW at a pulse repetition rate of 1 kHz focused into a spot with a diameter of 0.1 mm in the 10 mm long fused silica cell. The luminescence emitted in the forward direction was collected by reflective optics and focused with a spherical mirror onto the input slit of a spectrograph (Chromex 250) coupled to a streak camera (Hamamatsu 5680) equipped with a fast single sweep unit, M5676, with a temporal resolution of 2 ps. The convolution of a rectangular streak camera slit in the sweep range of 250 ps with an electronic jitter of the streak camera trigger pulse provided a Gaussian (over 4 decades) temporal apparatus function with a FWHM of 20 ps.

Emission decay curves for hybrid materials

To study processes of charge transport in hybrid materials, films were formed on thin glass plates as follows: 1–2 mg of the hybrid material was added to 200 μL of *n*-butanol in an Eppendorf tube, the tube was placed in an ultrasonic bath for 1–2 minutes, then the suspension was applied on the glass and dried on the tile surface preheated to 50 °C. The obtained films were investigated *via* time resolved luminescence spectroscopy in transmission mode (not in diffuse reflection mode).

Electrochemistry studies

Electrochemical measurements were carried out at 22 °C with an IPC-ProM potentiostat. Cyclic voltammetry experiments were performed in a 1.0 mL cell equipped with a glassy carbon (GC) electrode (disk d = 2 mm), Ag/AgCl/KCl (aq. saturated; reference electrode), and a platinum electrode (counter electrode). Compounds were dissolved in degassed dry CH_3CN or DMF containing TBAP as the supporting electrolyte (0.1 M). Dry argon gas was bubbled through the solutions for 30 min before cyclic voltammetry experiments. The scan rate was 200 mV s^{-1}.

X-ray photoelectron spectroscopy (XPS)

X-ray photoelectron spectroscopy (XPS) analysis was performed to understand the composition, chemical oxidation state of the ruthenium and also to uncover the chemical environment changes of the elements in the hybrid samples. The measurements were carried out on an XPS system (Thermo Fisher Scientific, Waltham, MA, USA) equipped with a hemispherical analyzer and using monochromatic Al Kα radiation as an X-ray source (1486.7 eV). Data analysis was performed using Unifit software (v.2014, Leipzig, Germany), and background subtraction was done by the Shirley method. The core level signals from the elements were fitted using asymmetric and symmetric Gaussian–Lorentzian convolution functions. The positions of the peaks in the binding energy scale were calibrated to the C 1s peak corresponding to the carbon contamination of the surface (285.0 eV) with an accuracy of 0.1 eV.

Conclusions

The obtained results show that the surface modification of SnO_2 nanoparticles with polypyridine ruthenium complexes with imidazophenanthroline-containing ligands leads to an increase of conductivity upon the irradiation of organometallic complexes placed on the surface of semiconductor oxides. Conductivity arises as a result of the electron injection from the ^{3}MLCT of the organometallic complex into the conduction band of a semiconductor. More donor imidazophenanthroline

ligand in the complex causes more efficient electron injection. In the case of In_2O_3, the deposition of Ru(II) complexes leads to a decrease in conductivity, apparently due to the specific structure of the surface layer of the semiconductor.

Interfacial electron transfer is expected to depend sensitively on semiconductors because of the differences in conduction band electronic structures and band edge positions, which affect the electronic coupling strength to the adsorbate and the electron accepting state density in the conduction band.[89] Aside from TiO_2, electron injection dynamics to other metal oxide semiconductors have also been examined, although much less extensively.

The injection of electrons from the Ru^{2+} complex to the conducting band of SnO_2 and In_2O_3 has been proposed in some reports, see ref. 90–93. The different aspects of the adsorbate/semiconductor system have been explored in order to understand the importance of various factors in determining injection dynamics. Among them are the structure of Ru^{2+} complex itself[94] or design of bridging units between the chromophore and the surface of the semiconductor, as well as the nature of the semiconductor.[89] In article,[91] another way was proposed for electron injection efficiency modification, which consists in changing the energy gap between the pseudo-Fermi level of SnO_2 and the oxidation potential of the excited sensitizer by an externally applied electrochemical bias. For SnO_2 and In_2O_3, it was found that the electron injection rate depends on the total available accepting states in the semiconductor as well as electronic coupling and reorganization energy.[93,95] Several studies have shown that electron transfer from ruthenium complexes to modified tin oxide electrodes can be used to create pH sensors and molecular switches.[96,97]

Because of the high nanoparticle surface area, a large density of defect states at the surface is expected, potentially affecting interfacial electron transfer. The important roles of trap states in the carrier transport within nanoparticles and back ET processes to adsorbates have been extensively studied for TiO_2, in a less extended form for Nb_2O_5 and ZrO_2 (for instance, ref. 89, 98 and 99) and increasingly for conductive nanoparticles.[100] Effects of defect states on electron injection have not been analyzed for modified samples of SnO_2 and In_2O_3. Thus, we first presented the experimental data on this matter.

Conflicts of interest

There are no conflicts to declare.

Acknowledgements

Financial support from the Russian Science Foundation (RSF No. 17-73-30036) and equipment facilities from the Center of collective facilities of the A. N. Nesmeyanov Institute of Organoelement compounds of Russian Ministry of Sciences and High Education are gratefully acknowledged. The mapping of element distribution was carried out using the equipment purchased by funds of Lomonosov Moscow State University Program of the Development (X-ray fluorescence spectrometer Tornado M4 plus).

References

1 K. Kalyanasundaram and M. Graetzel, *Coord. Chem. Rev.*, 1998, **77**, 347.
2 D. M. Roundhill, *Photochemistry and Photophysics of Metal Complexes in Modern Inorganic Chemistry*, Plenum Press, New York, 1994.
3 K. Kalyanasundaram, *Coord. Chem. Rev.*, 1982, **46**, 159.
4 A. J. Bard and M. A. Fox, *Acc. Chem. Res.*, 1995, **28**, 141.
5 N. Sutin and C. Creutz, *Pure Appl. Chem.*, 1980, **52**, 2717.
6 M. J. Cook, A. P. Lewis, G. S. G. McAuliffe, V. Skarda, A. J. Thomson, J. L. Glasper and D. J. Robbins, *J. Chem. Soc., Perkin Trans. 2*, 1984, 1303.
7 I. M. M. de Carvalho, I. de Sousa Moreira and M. H. Gehlen, *Inorg. Chem.*, 2003, **42**, 1525.
8 N. Kitamura, Y. Kawanishi and S. Tazuke, *Chem. Phys. Lett.*, 1983, **97**, 103.
9 D. P. Rillema, G. Allen, T. J. Meyer and D. Conrad, *Inorg. Chem.*, 1983, **22**, 1617.
10 H. B. Ross, M. Boldaji, D. P. Rillema, C. B. Blanton and R. P. White, *Inorg. Chem.*, 1989, **28**, 1013.
11 D. J. Manuel, D. P. Strommen, A. Bhuiyan, M. Sykora and J. R. Kincaid, *J. Raman Spectrosc.*, 1998, **28**, 933.
12 S. Ernst and W. Kaim, *Angew. Chem., Int. Ed. Engl.*, 1985, **24**, 430.
13 S. Ernst and W. J. Kaim, *Inorg. Chem.*, 1989, **28**, 1520.
14 Y. J. Bing, L. M. Leung and G. Menglian, *Tetrahedron Lett.*, 2004, **45**, 6361.
15 P. A. Anderson, F. R. Keene, T. J. Meyer, J. A. Moss, G. F. Strouse and J. A. Treadway, *Dalton Trans.*, 2002, 3820.
16 G. F. Strouse, J. R. Schoonover, R. Duesing, S. Boyde, W. E. Jones Jr. and T. J. Meyer, *Inorg. Chem.*, 1995, **34**, 473.
17 F. Xu, Y. X. Peng, B. Hu, T. Tao and W. Huang, *CrystEngComm*, 2012, **14**, 8023.
18 M. Stephenson, C. Reichardt, M. Pinto, M. Wachtler, T. Sainuddin, G. Shi, H. Yin, S. Monro, E. Sampson, B. Dietzek and S. A. McFarland, *J. Phys. Chem. A*, 2014, **118**, 10507.
19 C. Reichardt, M. Pinto, M. Wachtler, M. Stephenson, S. Kupfer, T. Sainuddin, J. Guthmuller, S. A. McFarland and B. Dietzek, *J. Phys. Chem. A*, 2015, **119**, 3986.
20 W. Pu and W. Lisha, *Inorg. Chim. Acta*, 2015, **436**, 45.
21 L. Chen, S. Sun, J. Li and Z. Fang, *Inorg. Chim. Acta*, 2016, **446**, 24.
22 F. Heinemann, J. Karges and G. Gasser, *Acc. Chem. Res.*, 2017, **50**, 2727.
23 J. Liu, C. Zhang, T. W. Rees, L. Ke, L. Ji and H. Chao, *Coord. Chem. Rev.*, 2018, **363**, 17.
24 L. K. McKenzie, H. E. Bryant and J. A. Weinstein, *Coord. Chem. Rev.*, 2019, **379**, 2.
25 A. Hogfeldt and M. Grätzel, *Chem. Rev.*, 1995, **95**, 49.
26 S. Ferrere and B. A. Gregg, *J. Am. Chem. Soc.*, 1998, **120**, 843.
27 Y. Chen, Q. Meng, L. Zhang, C. Han, H. Gao, Y. Zhang and H. Yan, *J. Energy Chem.*, 2018, **35**, 144.
28 D. Noukakis, M. van der Auwaraer and F. C. De Schryver, *J. Phys. Chem.*, 1994, **98**, 11745.
29 W. Ford and M. A. J. Rodjers, *J. Phys. Chem.*, 1995, **99**, 5139.
30 D. Liu and P. Kamat, *J. Electrochem. Soc.*, 1995, **142**, 835.

31 L. Tan-Sien-Hee and A. K. de Mersmaeker, *J. Electroanal. Chem.*, 1996, **406**, 147.
32 F. Fungo, L. A. Otero, L. Sereno, J. J. Silber and E. N. Durantidi, *J. Mater. Chem.*, 2000, **10**, 645.
33 S. Ferrere, A. Zaban and B. A. Gregg, *J. Phys. Chem. B*, 1997, **101**, 4490.
34 C. Nasr, P. Kamat and S. Hotchandani, *J. Phys. Chem. B*, 1998, **102**, 10047.
35 K. Hara, T. Horiguchi, T. Kinoshita, K. Sayama, H. Sugihara and H. Arakawa, *Sol. Energy Mater. Sol. Cells*, 2000, **64**, 115.
36 D. N. Srivastava, S. Chappel, O. Palchik, A. Zaban and A. Gedanken, *Langmuir*, 2002, **18**, 4160.
37 K. Tennakone, P. K. M. Bandaranayake, P. V. V. Jayaweera, A. Konno and G. R. R. A. Kumara, *Physica E*, 2002, **14**, 190.
38 H. Tian, P.-H. Liu, F.-S. Meng, E. Gao and S. Cai, *Synth. Met.*, 2001, **121**, 1557.
39 S. Chappel and A. Zaban, *Sol. Energy Mater. Sol. Cells*, 2002, **71**, 141.
40 A. Kay and M. Grätzel, *Chem. Mater.*, 2002, **14**, 2930.
41 X. Duan, Y. Huang and C. M. Lieber, *Nano Lett.*, 2002, **2**, 487.
42 C. Li, W. Fan, B. Lei, D. Zhang, S. Han, T. Tang, X. Liu, Z. Liu, S. Asano, M. Meyyappan, J. Han and C. Zhou, *Appl. Phys. Lett.*, 2004, **84**, 1949.
43 C. Li, W. Fan, D. A. Straus, B. Lei, S. Asano, D. Zhang, J. Han, M. Meyyappan and C. Zhou, *J. Am. Chem. Soc.*, 2004, **126**, 7750.
44 Y.-H. Kim, C.-H. Chung, J. Moon, S.-J. Lee, G. H. Kim and Y.-H. Song, *ETRI J.*, 2008, **30**, 308.
45 G. Benko, J. Kallioinen, P. Myllyperkio, F. Trif, J. E. I. KorppiTommola, A. P. Yartsev and V. Sundstrom, *J. Phys. Chem. B*, 2004, **108**, 2862.
46 R. H. Zheng, H. C. Guo, H. J. Jiang, K. H. Xu, B. B. Liu, W. L. Sun and Z. Q. Shen, *Chin. Chem. Lett.*, 2010, **21**, 1270.
47 R. M. F. Batista, S. P. G. Costa, M. Belsley, C. Lodeiro and M. M. M. Raposo, *Tetrahedron*, 2008, **64**, 9230.
48 X. Zhang, L. L. Li and Y. Liu, *Mater. Sci. Eng., C*, 2016, **59**, 916.
49 Z. Li, H. Yang, A. Zhang, H. Luo and K. Wanga, *Inorg. Chim. Acta*, 2011, **370**, 132.
50 J.-Z. Wu, B.-H. Ye, L. Wang, L.-N. Ji, J.-Y. Zhou, R.-H. Li and Z.-Y. Zhouc, *J. Chem. Soc., Dalton Trans.*, 1997, 1395.
51 M. R. Reddy, P. V. Reddy, Y. P. Kumar, A. Shrishailam, N. Nambigari and S. Satyanarayana, *J. Fluoresc.*, 2014, **24**, 803.
52 Z.-S. Li, H.-X. Yang, A.-G. Zhang, H. Luo and K.-Z. Wang, *Inorg. Chim. Acta*, 2011, **370**, 132.
53 L. F. Tan, F. Wang and H. Chao, *Helv. Chim. Acta*, 2007, **90**, 205.
54 G. Ginocchietti, E. Cecchetto, L. De Cola, U. Mazzucato and A. Spalletti, *Chem. Phys.*, 2008, **352**, 28.
55 E. Ioachim, E. A. Medlycott, G. S. Hanan, F. Loiseau and S. Campagna, *Inorg. Chim. Acta*, 2006, **359**, 766.
56 F. Monti, U. Hahn, E. Pavoni, B. Delavaux-Nicot, J.-F. Nierengarten and N. Armaroli, *Polyhedron*, 2014, **82**, 122.
57 A. N. Watkins, B. R. Wenner, J. D. Jordan, W. Y. Xu, J. N. Demas and F. V. Bright, *Appl. Spectrosc.*, 1998, **52**, 750.
58 Y. Tang, E. C. Tehan, Z. Tao and F. V. Bright, *Anal. Chem.*, 2003, **75**, 2407.
59 R. M. Bukowski, R. Ciriminna, M. Pagliaro and F. V. Bright, *Anal. Chem.*, 2005, **77**, 2670.
60 S. A. Denisov, S. Yu, J.-L. Pozzo, G. Jonusauskas and N. D. McClenaghan, *ChemPhysChem*, 2016, **17**, 1794.
61 M. Li, J. Liu, L. Sun, J. Pan and C. Zhao, *J. Organomet. Chem.*, 2008, **693**, 46.
62 Yu. H. Budnikova, S. A. Krasnov, I. M. Magdeev and O. G. Sinyashin, *ECS Trans.*, 2010, **25**, 7.
63 J. Robertson, *J. Phys. C: Solid State Phys.*, 1979, **12**, 4767.
64 M. Rumyantseva, A. Nasriddinov, S. Vladimirova, S. Tokarev, O. Fedorova, I. Krylov, K. Drozdov, A. Baranchikov and A. Gaskov, *Nanomaterials*, 2018, **8**, 671.
65 O. Bierwagen, *Semicond. Sci. Technol.*, 2015, **30**, 024001.
66 R. L. Weiher and R. P. Ley, *J. Appl. Phys.*, 1966, **37**, 299.
67 S. Das and V. Jayaraman, *Prog. Mater. Sci.*, 2014, **66**, 112.
68 S. Arooj, T. Xu, X. Hou, Y. Wang, J. Tong, R. Chu and B. Liu, *RSC Adv.*, 2018, **8**, 11828.
69 J. Gan, X. Lu, J. Wu, S. Xie, T. Zhai, M. Yu and Y. Tong, *Sci. Rep.*, 2013, **3**, 1021.
70 D. Braun, V. Scherer, C. Janowitz, Z. Galazka, R. Fornari and R. Manzke, *Phys. Status Solidi A*, 2014, **211**, 59.
71 P. D. C. King, T. D. Veal, D. J. Payne, A. Bourlange, R. G. Egdell and C. F. McConville, *Phys. Rev. Lett.*, 2008, **101**, 116808.
72 E. Korhonen, F. Tuomisto, O. Bierwagen, J. S. Speck and Z. Galazka, *Phys. Rev. B: Condens. Matter Mater. Phys.*, 2014, **90**, 245307.
73 J. D. Prades, J. Arbiol, A. Cirera, J. R. Morante, M. Avella, L. Zanotti and G. Sberveglieri, *Sens. Actuators, B*, 2007, **126**, 6.
74 M. G. Hosseini and E. Shahryari, *Ionics*, 2019, **25**, 2383.
75 G. Liu, W. Jaegermann, J. He, V. Sundstrom and L. Sun, *J. Phys. Chem. B*, 2002, **106**, 5814.
76 D. J. Morgan, *Surf. Interface Anal.*, 2015, **47**, 1072.
77 K. Jarzembska, S. Seal, K. Wozniak, A. Szadkowska, M. Bieniek and K. Grela, *ChemCatChem*, 2009, **1**, 144.
78 K. S. Kim and N. J. Winograd, *J. Catal.*, 1974, **35**, 66.
79 G. E. Muilenburg, *Handbook of X-Ray Photoelectron Spectroscopy*, PerkinElmer, Eden Prairie, 1979.
80 K. Zhang, D. Bin, B. Yang, C. Wang, F. Ren and Y. Du, *Nanoscale*, 2015, **7**, 12445.
81 C. L. Bianchi, V. Ragaini and M. G. Cattania, An XPS study on ruthenium compounds and catalysts, *Mater. Chem. Phys.*, 1991, **29**, 297–306.
82 D. Rocheforta, P. Daboa, D. Guaya and P. M. A. Sherwood, *Electrochim. Acta*, 2003, **48**, 4245.
83 V. Mazzieria, F. Coloma-Pascualb, A. Arcoyac, P. C. L'Argentièrea and N. S. Fígoli, *Appl. Surf. Sci.*, 2003, **210**, 222.
84 T. Sahm, A. Gurlo, N. Barsan and U. Weimar, *Sens. Actuators, B*, 2006, **118**, 78.
85 I. J. Lee and C. J. Yu, *J. Korean Phys. Soc.*, 2006, **49**, 2176.
86 Y. Wang, G. Duan, Y. Zhu, H. Zhang, Z. Xu, Z. Dai and W. Cai, *Sens. Actuators, B*, 2016, **228**, 74.
87 J. Stankiewicz, F. Villuendas, M. P. Lozano and I. Diez, *J. Appl. Phys.*, 2013, **114**, 083703.
88 A. Chizhov, M. Rumyantseva, R. Vasiliev, D. Filatova, K. Drozdov, I. Krylov, A. Marchevsky, O. Karakulina, A. Abakumov and A. Gaskov, *Thin Solid Films*, 2016, **618**, 253.

89 N. A. Anderson and T. Lian, *Annu. Rev. Phys. Chem.*, 2005, **56**, 491.
90 R. Memming, F. Schroppel and U. Bringmann, *J. Electroanal. Chem.*, 1979, **100**, 307.
91 P. V. Kamat, I. Bedja, S. Hotchandani and L. K. Patterson, *J. Phys. Chem.*, 1996, **100**, 4900.
92 T. Stergiopoulos, I. M. Arabatzis, H. Cachet and P. Falaras, *J. Photochem. Photobiol., A*, 2003, **155**, 163.
93 J. Guo, D. Stockwell, X. Ai, C. She, N. A. Anderson and T. Lian, *J. Phys. Chem. B*, 2006, **110**, 5238.
94 I. Ortmans, C. Moucheron and A. Kirsch-De Mesmaeker, *Coord. Chem. Rev.*, 1998, **168**, 233.
95 C. She, N. A. Anderson, J. Guo, F. Liu, W. Goh, D.-T. Chen, D. L. Mohler, Z.-Q. Tian, J. Hupp and T. Lian, *J. Phys. Chem. B*, 2005, **109**, 19345.
96 R. J. Forster, Y. Pellegrin and T. E. Keyes, *Electrochem. Commun.*, 2007, **9**, 1899.
97 L. X. Xue, Z. M. Duan, J. Jia, K. Z. Wang and M. A. Haga, *Electrochim. Acta*, 2014, **146**, 776.
98 J. Nelson, S. A. Haque, D. R. Klug and J. R. Durrant, *Phys. Rev. B: Condens. Matter Mater. Phys.*, 2001, **63**, 205321.
99 R. Huber, S. Spörlein, J. E. Moser, M. Grätzel and J. Wachtveitl, *J. Phys. Chem. B*, 2000, **104**, 8995.
100 R. J. Forster and T. E. Keyes, *Coord. Chem. Rev.*, 2009, **253**, 1833.